



# Aqueous solubility of Zn incorporated into Mg-Al-layered double hydroxides

Anna Dabizha · Michael Kersten

Accepted: 11 December 2021  
© The Author(s) 2022

**Abstract** Hydrotalcite minerals are layered double hydroxides (LDH) which play an important role in immobilizing hazardous compounds to decontaminate industrial wastewaters. The stability of an LDH is mostly evaluated in terms of its low solubility in water. However, the solubility of divalent trace metals immobilized by Mg-Al-type LDHs is not well known. Hydrotalcites containing Zn in solid solution, (Mg+Zn)<sub>3</sub>-Al-LDH, were synthesized by alkaline co-precipitation. A series of eleven LDH phases with Zn mole fractions  $X_{Zn} = Zn/(Mg+Zn)$  of 0–1 were characterized by powder X-ray diffractometry (XRD), Fourier-transform infrared (FTIR) spectroscopy, thermogravimetry (TGA), scanning and transmission electron microscopy (SEM/TEM), Brunauer-Emmett-Teller (BET) surface area analysis, and inductively coupled plasma mass (ICP-MS) spectrometry. The XRD analysis provided sharp characteristic spacings for  $d_{003}$  and  $d_{006}$  which occurred for all samples, confirming a layered LDH structure. Cell parameters ( $a$ ,  $c$ ) obeyed Vegard's law and confirmed the formation of a regular solid-solution series without a mixing gap. An aqueous equilibrium time

was determined by kinetic dissolution experiments. Steady-state solubility occurred after 120 days, but the experiments continued up to 240 days. The XRD and SEM/TEM analyses indicated no phase changes during the long-term dissolution experiments; neither were phase impurities detected after 240 days. The solubility products of the Mg- and Zn-bearing endmember compositions were calculated from experimentally determined total cation and anion concentrations using the *Visual Minteq* code for considering element speciation and ion pairing. The solubility product decreased as the Zn mole fraction increased, suggesting that the Zn-bearing LDH phases were more stable than the pure Mg<sub>3</sub>-Al-LDHs. Solid-solution aqueous-solution thermodynamic equilibrium modeling using the Lippmann “total solubility product” approach and applying Lippmann diagrams with logarithmic  $x$ -axes revealed a log-linear decrease in aqueous Zn solubility. The results are promising for remediation of metal-bearing liquid wastes because the metals that co-precipitated with the LDH were more strongly retained and, therefore, less soluble than the hydroxides or carbonates of the trace metal.

**Supplementary Information** The online version contains supplementary material available at <https://doi.org/10.1007/s42860-021-00169-y>.

A. Dabizha · M. Kersten (✉)  
Institut of Geosciences, Johannes Gutenberg University,  
Becherweg 21, 55099 Mainz, Germany  
e-mail: kersten@uni-mainz.de

**Keywords** LDH · Solid solution · Solubility product · SSAS · Thermodynamic equilibrium · Zinc

## Introduction

Hydrotalcites have the capability to immobilize hazardous compounds in waste deposits (Gade et al., 2000) and to decontaminate water (Ulibarri & Hermosín, 2006). They are also of increasing interest for use in cementitious solidification/stabilization systems of nuclear waste repositories, carbon capture, and green chemistry (Chaillot et al., 2021; Curtius et al., 2013). Their layered structure provides relatively large specific surface areas, meaning that they can sorb a wide range of anions and cations, including trace metals and other toxic inorganic contaminants. LDHs contain octahedral brucite-like  $\text{Mg}(\text{OH})_2$  layers in which one cation is bonded to six hydroxyl moieties, and one hydroxyl moiety is adjacent to three metal atoms in the hydroxyl layer (Drits & Bookin, 2006; Hofmeister & Von Platen, 1992). The layer-type lattice is due to the presence of relatively small two-fold positively charged cations close to the non-sphere symmetrical and highly polarizable  $\text{OH}^-$  ions (Cavani et al., 1991). The octahedra share edges to form sheets of large lateral extent, which are stacked and held together by hydrogen bonds (i.e. weak interactions). The OH-sheets may actually have two stacking sequences, rhombohedral and hexagonal (Cavani et al., 1991). The two forms can be distinguished by XRD (Drits & Bookin, 2006). Hydrotalcite crystallizes with a rhombohedral  $3R$  stacking sequence, the parameter of the unit cell being  $a$  and  $c = 3c'$ , where  $c'$  is the thickness of a stack consisting of one brucite-like sheet and one interlayer. Due to ordering of the Mg and Al cations and thus slight distortion of the octahedra, the LDH polytype form manasseite crystallizes with a hexagonal  $2H_1$  stacking sequence, the parameters of the unit cell being  $a$  and  $c = 2c'$  (Taylor, 1973; Cavani et al., 1991; Drits & Bookin, 2006). The divalent metal cations in LDHs can be replaced by isomorphous substitution for trivalent cations to give positive structural charges (Delgado et al., 2008), which is balanced by anions coordinating along the basal planes bounding the hydrated interlayer space. Such minerals, which are commonly termed anionic clays, have the ideal molecular formula  $[\text{M}(\text{II})_{1-x}\text{M}(\text{III})_x(\text{OH})_2]^{x+}(\text{A}^{n-})_{x/n} \cdot m\text{H}_2\text{O}$ , where  $A$  is one or several of an interlayer anion with valence  $n-$ , and  $x$  is the molar fraction of the substituting trivalent cation. The  $M(\text{III})$  cations that are mostly involved are Fe(III) and Al, the most

common  $M(\text{II})$  cations are Mg and Fe(II), and  $x$  typically lies between 0.25 and 0.33.

Three polytypes of Mg-bearing hydrotalcites are known. These are the ordered hydrotalcite type  $[\text{Mg}_6\text{Al}_3(\text{OH})_{18}][1.5\text{CO}_3 \cdot n\text{H}_2\text{O}]$ , the disordered hydrotalcite type  $[\text{Mg}_4\text{Al}_2(\text{OH})_{12}][\text{CO}_3 \cdot 3\text{H}_2\text{O}]$ , and the disordered or ordered manasseite type  $[\text{Mg}_6\text{Al}_2(\text{OH})_{16}][\text{CO}_3 \cdot n\text{H}_2\text{O}]$ . The natural manasseite (which was renamed hydrotalcite-2H in 2012) can undergo permanent interlayer anion exchange (Meyn et al., 1990). Carbonate is the most stable interlayer anion (Velu et al., 1997) but can be substituted reversibly by other anions such as (in order of increasing affinity)  $\text{OH}^-$ ,  $\text{Cl}^-$ ,  $\text{NO}_3^-$ , and  $\text{SO}_4^{2-}$  in a wide range of possible combinations (Constantino et al., 1995, 1998; Juan et al., 2004). However, this order of affinity is still under debate since being contested by other researchers such as Miyata (1983) and Bontchev et al. (2003), who observed reversed order of monovalent ion exchange preference of  $\text{Br}^- > \text{Cl}^- > \text{NO}_3^- > \text{I}^-$ . The high selectivity for halogens is favorably exploited, e.g. in water filters for  $\text{F}^-$  removal (Ren et al., 2021). In synthetic formulations, LDHs can incorporate isomorphously Zn, Cu, and Ni. The  $M(\text{II})/M(\text{III})$  ratio  $R = (1-x)/x$  is usually in the range  $1.5 < R < 4$  (Cavani et al., 1991; Chatelet et al., 1996). However, quantifying the mobilities of the intercalated hazardous compounds is difficult due to a lack of relevant published data.

In environmental assessment and industrial applications, the stability of LDHs is evaluated in terms of their low solubility in water. Aqueous solubilities of  $M(\text{II})_2$ -Al-type LDHs (Allada et al., 2006; Bocclair & Braterman, 1999; Johnson & Glasser, 2003) and  $M(\text{II})_3$ -Al-type LDHs (Curtius et al., 2013) have been reported. Thermodynamic calculations have shown that such LDHs can be formed even in water that is highly undersaturated with the individual divalent metal hydroxides and carbonates. The solubilities of these LDHs decrease in the order  $\text{Mg} > \text{Mn}(\text{II}) > \text{Co} > \text{Ni} > \text{Zn}$  for divalent cations, and  $\text{Al} > \text{Fe}(\text{III})$  for trivalent cations. The solubility products for the endmember compositions have been determined in previous studies. The solubilities of whole solid-solution series, however, have been investigated for only the hydrotalcite-pyroaurite system  $\text{Mg}_3(\text{Al}_x\text{Fe}^{\text{III}}_{1-x})(\text{CO}_3)_{0.5}(\text{OH})_8 \cdot n\text{H}_2\text{O}$  (Rozov et al., 2011) and the fougérite or “green rust” system  $\text{Mg}_y(\text{Fe}^{\text{II}}_x\text{Fe}^{\text{III}}_{1-x})(\text{CO}_3)_{x/2}(\text{OH})_2 \cdot n\text{H}_2\text{O}$  (Trolard & Bourrié, 2012;

Guilbaud et al., 2013). Both these solid-solution series contain trivalent Fe cations that are important in the natural environment. The solubilities of whole solid-solution series containing different divalent trace metal cations more relevant for industrial applications such as wastewater treatment in the metallurgical industry have not been published previously. The main aim of the present study was to investigate the effect of Zn substituted into the Mg<sub>3</sub>-Al-type LDH on the aqueous solubility. The results may serve as an example for quantification of the Cd and Pb immobilization, which are more toxic divalent trace metals. The main hypotheses were that: (1) a continuous solid-solution series can be formed followed by various analytical techniques (XRD, FTIR, TGA); and (2) the solubilities can be described by Lippmann solid-solution aqueous-solution (SSAS) thermodynamic equilibrium diagrams.

## Materials and Methods

Hydrotalcite with the formula [Mg<sub>3-x</sub>Zn<sub>x</sub>Al(OH)<sub>8</sub>](CO<sub>3</sub>)<sub>0.5</sub>·2H<sub>2</sub>O was used in this study. Carbonate was used as the anion because the Zn-LDHs containing CO<sub>3</sub><sup>2-</sup> are generally less soluble than Zn-LDHs containing other anions (Velu et al., 1997). Reagent-grade chemicals used in this study were (Al(NO<sub>3</sub>)<sub>3</sub>·9H<sub>2</sub>O, Mg(NO<sub>3</sub>)<sub>2</sub>·6H<sub>2</sub>O, NaCl, NaClO<sub>4</sub>, Na<sub>2</sub>CO<sub>3</sub>, NaNO<sub>3</sub>, NaOH, and Zn(NO<sub>3</sub>)<sub>2</sub>·6H<sub>2</sub>O), obtained from Honeywell Fluka Analytical (Seelze, Germany), and were used without further pre-treatment. MilliQ water was used in all experiments and analyses. All equipment was cleaned with 10% HNO<sub>3</sub> (Suprapure quality; Merck, Darmstadt, Germany) before use.

Mineralogical analysis of the samples was carried out using a 3000 TT X-ray powder diffractometer (Seifert, Ahrensburg, Germany); samples were analyzed before and after washing the co-precipitates and after the dissolution experiments to determine impurities. Each sample was scanned by applying CuK $\alpha$  radiation at 30 kV and 45 mA in continuous mode over the range 5 to 90°2 $\theta$  with a step size of 0.02°2 $\theta$  s<sup>-1</sup>. FTIR spectra of the solid samples were also acquired to determine the interlayer anion composition. For this, a 1–2 mg aliquot of a dried subsample was mixed with 200 mg of oven-dried, spectroscopic-grade KBr salt (refractive index 1.559, particle diameter 5–20  $\mu$ m), then the mixture was ground for 1 min. The mixture

was then pressed in a die with 8 t of pressure applied for 3–4 min to form a disc or pellet. Potential ion-exchange between the LDH and the KBr matrix was considered as negligible under the dry conditions, as the FTIR analysis was performed immediately after sample preparation. Triplicate FTIR spectra were acquired, each involving 100 scans recorded in the range 400 to 4000 cm<sup>-1</sup> at a resolution of 4 cm<sup>-1</sup>. The FTIR spectra were acquired using a 1725X FTIR spectrometer (PerkinElmer, Waltham, Massachusetts, USA). The BET specific surface areas of the samples were determined using a Quantachrome NOVA 1200 system (Anton Paar, Graz, Austria). The SEM and TEM images were acquired using a Philips 420 STEM instrument (Philips, Eindhoven, The Netherlands). The interlayer water, hydroxyl, and carbonate contents were assessed by TGA using an STA 409 EP system (Netzsch, Selb, Germany) with corundum (Al<sub>2</sub>O<sub>3</sub>) as a reference. The TGA was performed in the temperature range between 25 and 1000°C using an inert nitrogen atmosphere and a heating rate of 10°C min<sup>-1</sup>. The carbonate content was determined using a CSD-225 system (LECO, St. Joseph, Michigan, USA). To determine the cation content of a solid sample, a subsample of 4–10 mg was dissolved in 1% HNO<sub>3</sub> and the solution was then analysed by ICP-MS (Agilent 7500, Waldbronn, Germany).

**Table 1** Molar ratios used in the co-precipitation method to synthesize the LDH materials. Nitrate salts were used, and CO<sub>3</sub><sup>2-</sup> anions were provided by Na<sub>2</sub>CO<sub>3</sub>

LDH	Mg	Zn	Al	CO <sub>3</sub> <sup>2-</sup>	X <sub>Zn</sub>
SMZ1	1	0	0.34	0.15	0
SMZ2	0.9	0.1	0.34	0.15	0.1
SMZ3	0.8	0.2	0.34	0.15	0.2
SMZ4	0.7	0.3	0.34	0.15	0.3
SMZ5	0.6	0.4	0.34	0.15	0.4
SMZ6	0.5	0.5	0.34	0.15	0.5
SMZ7	0.4	0.6	0.34	0.15	0.6
SMZ8	0.3	0.7	0.34	0.15	0.7
SMZ9	0.2	0.8	0.34	0.15	0.8
SMZ10	0.1	0.9	0.34	0.15	0.9
SMZ11	0	1	0.34	0.15	1

## LDH Synthesis

Many preparation methods have been described previously (Chaillot et al., 2021; Theiss et al., 2016), but the constant-pH co-precipitation method using alkaline solutions is the most promising for synthesis of well crystalline hydrotalcite-like materials (Kloprogge et al., 2004). Hydrothermal and microwave treatments were not performed, which would usually cause formation of the LDHs with a  $M(\text{II})/\text{Al}$  ratio of 2:1 rather than 3:1 (Benito et al., 2008; Britto et al., 2007; Kloprogge et al., 2004). A mixture of stoichiometric amounts (Table 1) of Mg, Zn, and Al nitrate salt solutions (1.0 mol/L, 250 mL) was added at a rate of  $\sim 20 \text{ mL min}^{-1}$  to a 10% stoichiometric excess of 1 M  $\text{Na}_2\text{CO}_3$  solution stirred at 40°C. Regardless of the original  $M^{2+}/M^{3+}$  ratio, a white precipitate formed immediately after addition of the first drop of the metal salt solution to the basic  $\text{Na}_2\text{CO}_3$  solution. Before taking pH measurements, the WTW InoLab® Level 2 pH meter (Xylem Analytics, Weilheim, Germany) equipped with a SenTix 61 pH/Pt electrode was calibrated using 0.001 and 1.0 M KOH solutions. If the reaction mixture approached  $\text{pH } 10.0 \pm 0.5$ , 2.0 M NaOH was added simultaneously to the  $M^{2+}/M^{3+}$  mixture to keep the reaction mixture at pH 10. Having added all the salt solution, the reaction mixture was stirred vigorously at 40°C for 4 h. Once the reaction was complete, the suspension was cooled to room temperature, separated into a 50 mL centrifuge tube and centrifuged at  $3000 \times g$  for 20 min. A series of tubes of the pure  $\text{Mg}_3\text{-Al-LDHs}$  co-precipitates were kept in the mother liquor for up to 7 days, and the total dissolved Mg and Al concentrations were determined each day using one of the tubes. The supernatant was passed through a 0.2  $\mu\text{m}$  cellulose membrane filter (Sartorius, Göttingen, Germany) using a syringe. A few drops ( $\sim 0.1 \text{ mL}$  per 50 mL sample) of concentrated  $\text{HNO}_3$  were added to the filtrate and stored at 4°C until the filtrated solution could be analyzed for cation concentrations. The white precipitate remaining in the centrifuge tube was washed with 500 mL of deionized water at least five times to remove excess sodium, carbonate, and nitrate ions. The concentration of dissolved nitrate was determined by ion chromatography using a 761 Compact IC system (Metrohm, Herisau, Switzerland) to ensure that no original salt compounds remained prior to the dissolution experiments. The precipitate was then dried

on a glass plate at 50°C in an oven, ground to a fine powder in an agate mortar, and stored in a desiccator.

## Dissolution Experiments

A preliminary experiment using the pure  $\text{Mg}_3\text{Al-LDH}$  endmember was performed to determine the time required for equilibration. Six sets of such experiments were first prepared. For each experiment, 100 mg of LDH was added to 100 mL of an aqueous solution in a 50 mL polyethylene bottle, which was closed and shaken at 25°C to allow equilibration to occur. The ionic strength of the solution was fixed by adding 3 mM  $\text{Na}_2\text{CO}_3$  (30 mg/100 mL) to act as a background electrolyte well above the ambient  $\text{CO}_2$  contribution from the atmosphere. The solution was adjusted to  $\text{pH } 10.7 \pm 0.5$  by addition of 0.1 M NaOH. The total dissolved Mg and Al concentrations were determined at 20, 46, 123, 166, 202, and 240 days to allow determination of the time taken to reach equilibrium. As a result, the minimum time necessary to reach equilibrium was found to be 120 days. Three sets of 11 solid-solution samples of various Zn/Mg ratios, including blanks, were prepared and kept at 25°C for 240 days. All samples were centrifuged, and the supernatants passed through 0.2  $\mu\text{m}$  membrane filters before the solute concentrations determination. A 20 mL subsample each was left untreated, and the pH and anion content were determined. The dissolved residual carbonate content was determined (in duplicate) using a High TOC II total carbon analyser (Elementar Analysensysteme, Hanau, Germany). Another 5 mL part of each solute sample was diluted by a factor of 10 and the solution was acidified by adding 0.1 mL of concentrated  $\text{HNO}_3$  for stabilization of the cations. Divalent cation (Mg, Zn) concentrations were determined using an Agilent 7500 ICP-MS (Agilent, Waldbronn, Germany). The Al concentrations were determined in a last 10 mL subsample (again acidified by adding 0.1 mL of concentrated  $\text{HNO}_3$ ) using a NexION ICP-MS (PerkinElmer LAS, Rodgau, Germany) in dynamic reaction cell mode using  $\text{NH}_3$  as the cell gas to decrease CN interference with the Al response. Rh was added to act as an internal standard (100  $\mu\text{L}$  of  $1 \mu\text{g mL}^{-1}$  Rh). The instrument was tuned using a 10  $\text{ng mL}^{-1}$  multi-element standard (Merck XVI, which contained Li/Y/Ce/Tl). The Al detection limit thus achieved was  $10 \text{ nmol L}^{-1}$ .

## Results and Discussion

### Characteristics of Synthesized LDHs

The  $M(\text{II})/\text{Al}$  ratios of the washed samples were 3.24–3.69 and agreed well with the ratios for the initial solutions (Table 1), most of the differences being <20%. The greater than stoichiometric  $M(\text{II})/\text{Al}$  ratios may have been caused by some Al lixiviation during excessive washing. Obtaining materials with the desired compositions and exact stoichiometric carbonate contents was difficult, so reactant solutions containing 10% excess carbonate were used to make synthesis of LDHs with the desired compositions easier, albeit with somewhat greater than desired  $\text{CO}_3^{2-}$  contents as revealed by the TG analysis. The composition of the solid samples determined by chemical and TG analyses, as detailed in the Supplementary Material (Figs. S1 and S2), are shown in Table 2. Slight differences only were observed in the TGA curves between Mg–Al–LDH and Zn–Al–LDH endmembers, indicating that the thermal stabilities and temperatures required for the removal of interlayer water, dehydroxylation of the cationic layers, and removal of the interlayer carbonate anion were similar regardless of cation substitution. No alien anions such as  $\text{NO}_3^-$  were detected by the FTIR analysis (Figs. S3 and S4).

The BET surface areas between 20 and 90  $\text{m}^2 \text{g}^{-1}$  (Table 2) indicated nano-particulate characteristics of the material. The TEM images of the synthesized LDHs in fact showed nanoparticles of hexagonal

platy shape with diameters of  $\sim 100 \text{ nm}$  (Fig. S5a,b). The FTIR analyses revealed characteristic vibrations of Mg/Al-hydroxycarbonate phases. The FTIR spectra showed broad but intense hydroxyl stretching bands between 3400 and 3500  $\text{cm}^{-1}$ , and weak interlayer water molecule bending bands near 1620–1640  $\text{cm}^{-1}$ . The rather sharp intense band at 1360–1385  $\text{cm}^{-1}$  was caused by  $\nu_3$  anti-symmetric stretching of interlayer carbonate, shifted from its position in free  $\text{CO}_3^{2-}$  because of strong hydrogen bonding with hydroxyl groups and  $\text{H}_2\text{O}$  molecules in the interlayer space. The bands at  $<1000 \text{ cm}^{-1}$  were ascribed to both  $\nu_2$  and  $\nu_4$  modes of carbonate and to  $M\text{--OH}$  modes, respectively. An intense and sharp band near 450  $\text{cm}^{-1}$  was found in each sample and was assigned to polymerized

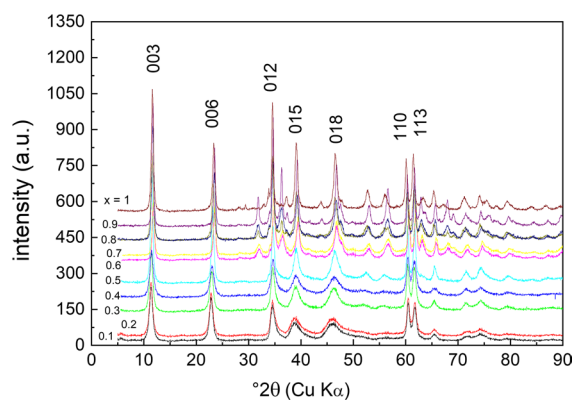


**Fig. 1** XRD patterns for hydrotalcite solid solutions synthesized using various Zn molar ratios

**Table 2** Chemical formulae of the synthesized LDH materials determined from the results of the chemical and TGA analyses and normalized to the Al content, and the BET surface areas of the materials indicating nano-crystalline characteristics of the materials

LDH	Formulae of LDH	$X_{\text{Zn}}$	(Mg+Zn)/Al	BET ( $\text{m}^2/\text{g}$ )
SMZ1	$[\text{Mg}_{3.48}\text{Al}(\text{OH})_{8.37}](\text{CO}_3)_{0.52} \cdot 2.09\text{H}_2\text{O}$	0.00	3.48	86.8
SMZ2	$[\text{Mg}_{3.07}\text{Zn}_{0.36}\text{Al}(\text{OH})_{8.31}](\text{CO}_3)_{0.52} \cdot 2.08\text{H}_2\text{O}$	0.10	3.42	48.1
SMZ3	$[\text{Mg}_{2.96}\text{Zn}_{0.73}\text{Al}(\text{OH})_{8.40}](\text{CO}_3)_{0.53} \cdot 2.10\text{H}_2\text{O}$	0.20	3.69	70.6
SMZ4	$[\text{Mg}_{2.57}\text{Zn}_{1.09}\text{Al}(\text{OH})_{8.38}](\text{CO}_3)_{0.52} \cdot 2.10\text{H}_2\text{O}$	0.30	3.66	54.4
SMZ5	$[\text{Mg}_{1.85}\text{Zn}_{1.22}\text{Al}(\text{OH})_{8.46}](\text{CO}_3)_{0.53} \cdot 2.11\text{H}_2\text{O}$	0.40	3.07	42.1
SMZ6	$[\text{Mg}_{1.83}\text{Zn}_{1.87}\text{Al}(\text{OH})_{8.75}](\text{CO}_3)_{0.55} \cdot 2.19\text{H}_2\text{O}$	0.51	3.70	70.2
SMZ7	$[\text{Mg}_{1.37}\text{Zn}_{2.05}\text{Al}(\text{OH})_{8.34}](\text{CO}_3)_{0.52} \cdot 2.08\text{H}_2\text{O}$	0.60	3.42	33.4
SMZ8	$[\text{Mg}_{1.0}\text{Zn}_{2.24}\text{Al}(\text{OH})_{8.70}](\text{CO}_3)_{0.54} \cdot 2.18\text{H}_2\text{O}$	0.69	3.24	56.1
SMZ9	$[\text{Mg}_{0.65}\text{Zn}_{2.85}\text{Al}(\text{OH})_{7.97}](\text{CO}_3)_{0.50} \cdot 1.99\text{H}_2\text{O}$	0.81	3.50	49.7
SMZ10	$[\text{Mg}_{0.3}\text{Zn}_{2.97}\text{Al}(\text{OH})_{7.89}](\text{CO}_3)_{0.49} \cdot 1.97\text{H}_2\text{O}$	0.91	3.27	37.3
SMZ11	$[\text{Zn}_{3.24}\text{Al}(\text{OH})_{8.55}](\text{CO}_3)_{0.53} \cdot 2.14\text{H}_2\text{O}$	1.00	3.24	26.8



$[\text{AlO}_6]^{3-}$  groups, and single groups with an Al–OH bond length of 0.161 nm typical for LDHs (SM).

The XRD patterns of all the synthesized LDHs contained features common in layered phases (e.g. narrow, symmetrical, and strong reflections at low  $^\circ 2\theta$  values and weaker, less symmetrical reflections at higher  $^\circ 2\theta$  values), as shown in Fig. 1. The hexagonal layer structure with sharp symmetrical peaks for the (003), (006), and (009) planes and broad but still symmetrical peaks for the (015) and (018) planes are characteristic of hydrotalcites (Hofmeister & Von Platen, 1992). A well crystalline phase resembling an LDH compound was the only solid phase prepared for the dissolution experiments in the washed samples, but the unwashed samples revealed some other diffractions during the co-precipitation syntheses. The

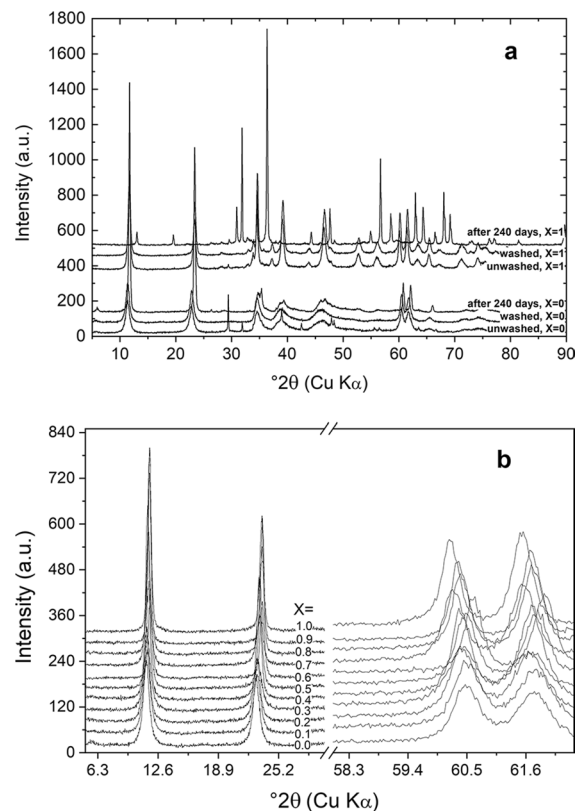


**Fig. 2** Powder X-ray diffractograms for the hydrotalcite solid-solutions with mole fraction of Zn = X, where **a** depicts the patterns for unwashed and washed original co-precipitates and samples collected from the equilibrium dissolution experiment after 240 days, and **b** the peaks characteristic for the LDH phases of various  $X_{\text{Zn}}$  contents used in the Vegard's law analysis

XRD patterns of the unwashed samples contained a diffraction near  $30^\circ 2\theta$  assigned to a  $\text{NaNO}_3$  phase; no nitrate diffraction was present after the washing treatment, however. A broad diffraction band was also present at  $48^\circ 2\theta$ , indicating a gibbsite ( $\text{Al}(\text{OH})_3$ ) impurity, which disappeared after 240 days of the dissolution experiment (Fig. 2a).

Crystallographic lattice parameters ( $a$ ,  $c$ ) were calculated for all LDH compounds synthesized with various Zn cation contents. The degree of crystallinity of each LDH sample was determined from the basal (003) and (006) reflection intensities and sharpness

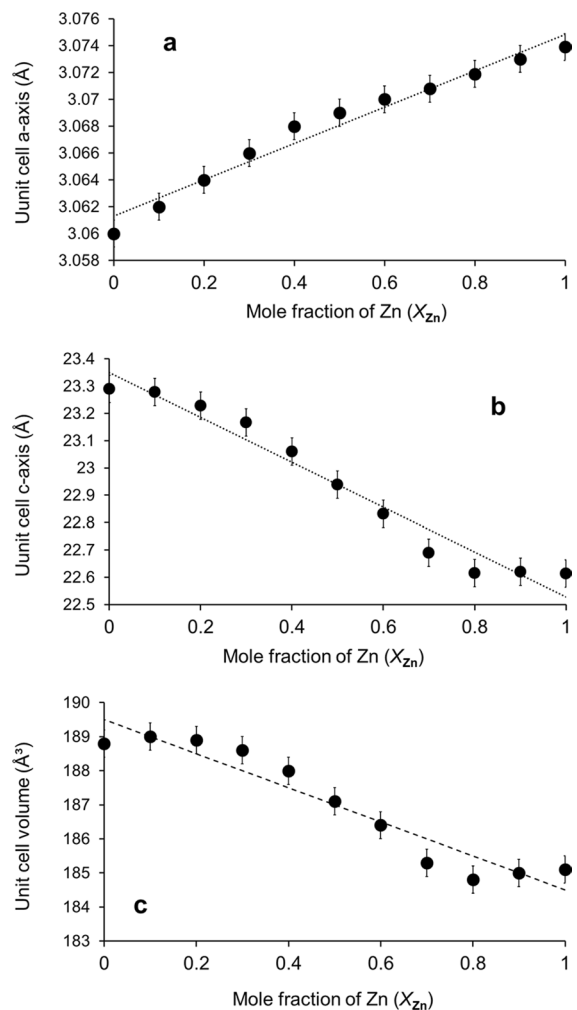


**Fig. 3** Values for the unit cell **a**  $a$ -axis, **b**  $c$ -axis, and **c** volumes determined by powder X-ray diffractometry for the LDH samples with various mole fractions of Zn used for the Vegard's law analysis. The dotted lines indicate linear correlations

(Fig. 2b). The broadening of the XRD peaks at 39 and 46°2θ was due to the statistical distribution of the layer stacking sequences of the 2H and 2R polytypes. The layer stacking faults do not affect significantly the distance between the brucite-like layers in the *c* axis direction, however, because LDH compounds commonly show no long-range ordering, i.e. the respective stacking sequences of the hexagonally or trigonally ordered endmembers are commonly randomly distributed in LDHs.

The lattice parameters were calculated (Fig. 3), in which *a* is the mean cation–cation distance in the brucite-like layer with  $a = 2d_{110}$ . The cell parameter *c* was determined from the equation  $c/3 = \frac{1}{2}\{d_{(003)} + 2d_{(006)}\}$ . The unit-cell volume *V* was calculated from the cell parameters using the equation  $V = a^2 c \sin(120)$ , which was simplified to  $(\sqrt{3}/2) a^2 c$ . Assuming that the brucite-like layer was 4.8 Å wide (Drezdzone, 1988), the interlayer space was 2.8 Å, in accordance with the locations of the carbonate anions with their molecular planes parallel to the brucite-like layers. Although of nearly the same ionic radius in octahedral coordination (Shannon, 1976), the inclusion of Zn into the Mg-bearing hydroxycarbonate slightly increased the cell parameter and shifted the peak position to lower 2θ values, therefore increasing the *d* spacing. However, Curtius et al. (2013) reported no elongation of the octahedra in the *c* direction by Rietveld analysis of XRD patterns in spite of increasing ionic radii of Ni < Mg and Co < Fe(II) of the LDH endmembers, which showed a lack of dependency on the ionic radius. Nonetheless, a clear linear correlation was found between the cell constants and cation composition ratios, as required by Vegard's law, even for the *c* direction (Fig. 3a and b), and thus also for the cell volume (Fig. 3c). The formation of the desired solid solutions without a mixing gap over the whole range of Mg-Zn-bearing hydroxycarbonate formulations was thus confirmed by the XRD analysis.

#### Aqueous Solubility Data and SSAS Equilibrium Experiments

As shown in Fig. 4a, apparent equilibrium was reached on the fifth day of the co-precipitation experiments. The Mg concentration was 1.2 μmol/L on that day and for the rest of the experiment. Somewhat lower equilibrium concentrations were reached after day 150 of the dissolution experiments

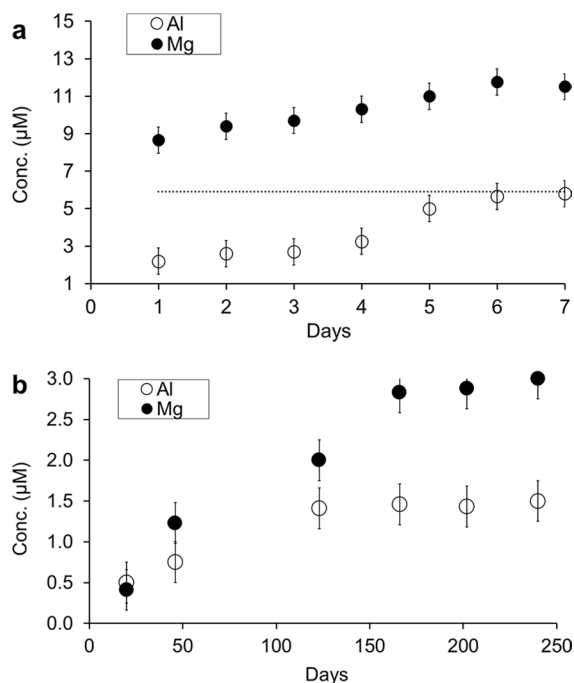
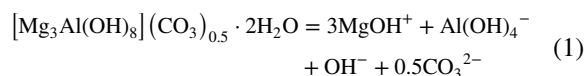


**Fig. 4** Measured total dissolved concentrations of Al and Mg for **a** the co-precipitation synthesis solution during the first 7 days of ageing at pH 10.0±0.5 (the dotted line indicates the Al concentration in the presence of gibbsite), and **b** the dissolution experiment after 240 days (pH 10.2±0.5)

(Fig. 4b). The approximately 3-fold different concentrations at equilibrium in the mother liquor were probably caused by some phase impurities, particularly gibbsite, as indicated by the XRD analysis. In principle, buffering of the Al is thus possible in order to avoid the tricky dissolved Al concentration measurements (Johnson & Glasser, 2003), but this approach was not preferred here because of the lack of a gibbsite impurity detected after 240 days in the dissolution experiments. A modified solubility constant for the pure Mg-LDH endmember with the ideal stoichiometry was calculated using the dissolution reaction:



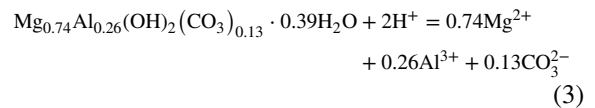
The solubility product was not formulated using the activities of the free cations as usual. It was defined by hydroxo-complexes  $\text{MgOH}^+$  and

$\text{Al}(\text{OH})_4^-$ , which removed the extreme surplus of  $\text{OH}^-$ . The  $\text{Al}(\text{OH})_4^-$  species concentration was, however, almost the same as the total Al concentration at  $\text{pH} > 10$ . The  $\text{MgOH}^+$  species concentrations were calculated using the geochemical speciation modeling code *Visual Minteq 3.1* with the built-in Davies equation for the ion activity product calculations from the default thermodynamic database (Gustafsson, 2020). The *Visual Minteq* simulation results indicated also that all aqueous solutions of the dissolution experiments analysed at day 240 were undersaturated with respect to any secondary mineral phases, including magnesite ( $\text{MgCO}_3$ ) and gibbsite. Equation (1) allowed the logarithmic solubility product to be formulated:

$$\log K_{\text{SP}, \text{Mg-LDH}} = 3 \log \{ \text{MgOH}^+ \} + \log \{ \text{Al}(\text{OH})_4^- \} + \log \{ \text{OH}^- \} + 0.5 \log \{ \text{CO}_3^{2-} \} \quad (2)$$

where the curved brackets indicate the activity of the respective ion. For the long-term steady state reached in the dissolution experiments after day 240, the dissolution of the LDHs gave almost the same Mg/Al ratios for the solutes and solids, indicating that almost congruent dissolution had occurred. For the pure  $\text{Mg}_3\text{-Al-LDH}$  endmember in this dissolution experiment (Fig. 4b), a  $\log K_{\text{SP}, \text{Mg-LDH}}$  of  $-32.2 \pm 0.2$  could be calculated from the ion activity product (Eq. 2). Even though it was for an uncommon solubility product formulation, this value can be translated using the

*Visual Minteq* code into another uncommon solubility product formulation to compare with the solubility of manasseite found in a previous study (Allada et al., 2006):



The logarithmic solubility product for this dissolution reaction was (Allada et al., 2006):

$$\log K_{\text{SP}, \text{Mg-LDH}}^* = 0.74 \log \{ \text{Mg}^{2+} \} + 0.26 \log \{ \text{Al}^{3+} \} + 0.13 \log \{ \text{CO}_3^{2-} \} + 2\text{pH} = 9.82 \quad (4)$$

Using the same formulation, the present study gave a  $\log K_{\text{SP}, \text{Mg-LDH}}^*$  of 9.45, which corresponded to the uncertainty for the value found by Allada et al. (2006). Rozov et al. (2011) calculated a traditional thermodynamic solubility product using the stoichiometric free ion activity product equation:

$$\log K_{\text{SP}, \text{Mg-LDH}}^* = 3 \log \{ \text{Mg}^{2+} \} + \log \{ \text{Al}^{3+} \} + 0.5 \log \{ \text{CO}_3^{2-} \} + 8 \log \{ \text{OH}^- \} = -68.9 \quad (5)$$

Using this formulation, the present dissolution experiment gave a  $\log K_{\text{SP}, \text{Mg-LDH}}^*$  of  $-73.4$ , which was somewhat lower than the value found by Rozov et al. (2011). However, Eq. 5 is quite sensitive to pH, meaning that even a minor uncertainty in the pH drastically increased uncertainty in the calculated  $\log K_{\text{SP}, \text{Mg-LDH}}^*$ . For

**Table 3** Ion concentrations found after 240 days of the aqueous solubility experiments using the LDH materials of various mole fractions of Zn ( $X_{\text{Zn}}$ )

LDH	$X_{\text{Zn}}$	pH	Mg ( $\mu\text{mol/L}$ )	Zn ( $\text{nmol/L}$ )	Al ( $\mu\text{mol/L}$ )	$\text{CO}_3^{2-}$ ( $\text{mmol/L}$ )
SMZ1	0.00	10.1	$3.08 \pm 0.10$	-	$1.44 \pm 0.05$	$2.7 \pm 0.6$
SMZ2	0.10	10.7	$1.28 \pm 0.06$	$24 \pm 2$	$0.46 \pm 0.03$	$2.7 \pm 0.4$
SMZ3	0.20	10.8	$1.05 \pm 0.05$	$29 \pm 4$	$0.38 \pm 0.04$	$2.8 \pm 0.2$
SMZ4	0.30	10.8	$1.02 \pm 0.05$	$52 \pm 6$	$0.37 \pm 0.03$	$2.7 \pm 0.4$
SMZ5	0.40	11.6	$0.49 \pm 0.02$	$96 \pm 8$	$0.18 \pm 0.03$	$2.7 \pm 0.9$
SMZ6	0.51	11.3	$0.66 \pm 0.03$	$159 \pm 5$	$0.23 \pm 0.05$	$2.9 \pm 0.4$
SMZ7	0.60	11.2	$0.48 \pm 0.01$	$225 \pm 6$	$0.22 \pm 0.09$	$2.7 \pm 0.2$
SMZ8	0.69	11.2	$0.37 \pm 0.01$	$239 \pm 7$	$0.23 \pm 0.02$	$2.9 \pm 0.8$
SMZ9	0.81	11.1	$0.25 \pm 0.01$	$395 \pm 7$	$0.23 \pm 0.04$	$3.5 \pm 0.9$
SMZ10	0.91	11.5	$0.12 \pm 0.06$	$667 \pm 3$	$0.26 \pm 0.02$	$2.8 \pm 0.2$
SMZ11	1.00	10.5	-	$886 \pm 7$	$0.24 \pm 0.01$	$3.3 \pm 0.4$



example, an uncertainty of 0.5 pH units (e.g. between 10.0 and 10.5) would explain the 4 units difference. Corroborating the results against previously published data confirmed the present data as promising to be used for further modeling.

To formulate a binary SSAS equilibrium model, the solubility products of the other pure endmember assumed to form the solid solution first had to be determined using the formulation:

$$\log K_{SP, Zn-LDH} = 3 \log \{ZnOH^+\} + \log \{Al(OH)_4^-\} + \log \{OH^-\} + 0.5 \log \{CO_3^{2-}\} \quad (6)$$

The solubility constant for the dissolution experiment after day 240 (sample SMZ11 in Table 3) calculated using Eq. 6 was  $\log K_{SP, Zn-LDH} = -37.7 \pm 0.6$  and, therefore, more than five units lower than for the pure Mg endmember.

Thermodynamic equilibrium in the binary (Mg+Zn)<sub>3</sub>-Al-LDH system was described by the equivalence of the chemical potentials of the solid and aqueous phase components, i.e. by the mass action expressions:

$$\{ZnOH^+\}^3 \{Al(OH)_4^-\} \{OH^-\} \{CO_3^{2-}\}^{0.5} = K_{SP, Zn-LDH} X_{Zn-LDH} \lambda_{Zn-LDH} \quad (7)$$

and:

$$\{MgOH^+\}^3 \{Al(OH)_4^-\} \{OH^-\} \{CO_3^{2-}\}^{0.5} = K_{SP, Mg-LDH} (1 - X_{Zn-LDH}) \lambda_{Mg-LDH} \quad (8)$$

The solid-phase activities were given as the products of the appropriate mole fraction  $X$  and activity coefficient  $\lambda$ . Dividing Eq. 7 by Eq. 8 and removing the common ions gave the Berthelot–Nernst distribution law:

$$X_{Zn-LDH} / (1 - X_{Zn-LDH}) = D \{ZnOH^+\} / \{MgOH^+\} \quad (9)$$

where the Berthelot–Nernst distribution coefficient  $D$  is given by:

$$D = K_{SP, Mg-LDH} \lambda_{Mg-LDH} / K_{SP, Zn-LDH} \lambda_{Zn-LDH} \quad (10)$$

Equation 9 is the classic expression for a SSAS system at thermodynamic equilibrium. Another expression for SSAS equilibrium can be obtained by simply adding together Eqs. 7 and 8 to give:

$$\Sigma \Pi_{eq} = (\{ZnOH^+\} + \{MgOH^+\}) \{Al(OH)_4^-\} \{OH^-\} \{CO_3^{2-}\}^{0.5}, \quad (11)$$

where the term on the left-hand side is the “total solubility product” variable  $\Sigma \Pi$ , which is related via the expression on the right-hand side to give the total solubility product constant  $\Sigma \Pi_{eq}$  at thermodynamic equilibrium with the aqueous solute composition (Glynn & Reardon, 1990; Lippmann, 1980). Unlike the endmember solubility product  $K_{SP}$ , which remains constant regardless of the composition of the aqueous phase (at stoichiometric saturation with a given solid solution composition),  $\Sigma \Pi_{eq}$  varies as a function of the solid solution composition in terms of the fraction  $X_{Zn-LDH}$  of the trace metal in the host LDH phase. The  $\Sigma \Pi_{eq}$  constant can be calculated from the measured solute concentrations using Eq. 11. Alternatively,  $\Sigma \Pi_{eq}$  can be calculated if the activity fractions of the substituting cation in the aqueous phase at thermodynamic equilibrium are known. The solute activity fractions for the (Mg,Zn)<sub>3</sub>-Al-LDH system were defined as:

$$\chi_{Zn, aq} = \{ZnOH^+\} / (\{ZnOH^+\} + \{MgOH^+\}) \quad (12)$$

and:

$$\chi_{Mg, aq} = \{MgOH^+\} / (\{ZnOH^+\} + \{MgOH^+\}) \quad (13)$$

Substituting these two equations into Eq. 11 and rearranging the equation to express the activities of the solid-phase components in terms of their activity coefficients and mole fractions gives:

$$\Sigma \Pi_{eq} = \frac{1}{\frac{\chi_{Zn, aq}}{K_{SP, Zn-LDH} \lambda_{Zn-LDH}} + \frac{\chi_{Mg, aq}}{K_{SP, Mg-LDH} \lambda_{Mg-LDH}}} \quad (14)$$

In principle, Lippmann  $\Sigma \Pi$ - $X$ - $\chi$  phase diagrams can be constructed using the total solubility product Eqs. 11 and 14 and the appropriate mole and activity fractions (or solute concentrations) as coordinates (Lippmann, 1980). Analogous to phase diagrams for binary gas or binary liquid systems or for solid/melt systems, a Lippmann phase diagram is a plot of a solidus curve (the total solubility product defined by Eq. 11) and a solutus curve (the isothermal crystallization curve defined by Eq. 14) with the variable  $\Sigma \Pi$  as the ordinate. The solidus and solutus curves both form a characteristic loop that is common in phase diagrams involving the (complete) solubility of two phases in each other. The loop became wider as the difference between the

solubility products of the endmembers increased. The  $\log K_{SP}$  values for the endmembers were five units different, so a considerable loop opening was expected to indicate non-ideal SSAS equilibrium behavior.

A Lippmann diagram differs from a traditional phase diagram in that it uses aqueous activity products and activity fractions rather than element concentrations and mole fractions to define the compositions of all phases in the system. Two different scales were used for the abscissa, an activity-fraction scale  $\chi_{Zn,aq}$  relating to the aqueous-phase composition and a mole-fraction scale  $X_{Zn-LDH}$  defining the solid-phase composition. The activity-fraction scale required a degree of ion pairing and/or complexation with other ions in the aqueous solution to be considered. The effect of speciation is important in alkaline solutions of cementitious solidification/stabilization systems (e.g. Kulik & Kersten, 2002) in which cations that form complete or almost complete solid-solution series may not have similar aqueous complexing affinities, as in this case for Mg and Zn. A speciation model of ion complexation in the aqueous solution, such as the *Visual Minteq* code used here, was therefore required to construct Lippmann diagrams from experimental concentration data. The solidus and solutus curves were then plotted and used to predict the solubility of any solid solution at thermodynamic equilibrium. This was done in a similar way to phase diagrams used for binary solid/melt systems but with solutus instead of liquidus curves to give the solid-phase and aqueous-phase compositions for the series of possible thermodynamic SSAS equilibrium states.

For  $\{ZnOH^+\} \ll \{MgOH^+\}$  at  $pH > 10$ , Eq. 14 can be simplified in logarithmic terms to:

$$\log \Sigma \Pi_{eq} = -\log \chi_{Zn,aq} + \log \lambda_{Zn-LDH} - 37.7 \quad (15)$$

As discussed below, the term  $\log \lambda_{Zn-LDH}$  is small and can, therefore, be neglected at first approximation. However, because  $\{ZnOH^+\} \ll \{MgOH^+\}$  at  $pH > 10$ , all the  $\chi_{Zn,aq}$  values are  $< 0.01$  and a reliable solutus cannot easily be plotted on a linear  $\chi_{Zn,aq}$  scale, as is common in Lippmann diagrams (Fig. 5a). When plotting the  $\chi_{Zn,aq}$  values on a logarithmic scale, however, all the  $\chi_{Zn,aq}$  values for the dissolution experiment data were in fact on a perfectly straight line between the endmember solubilities (Fig. 5b), in

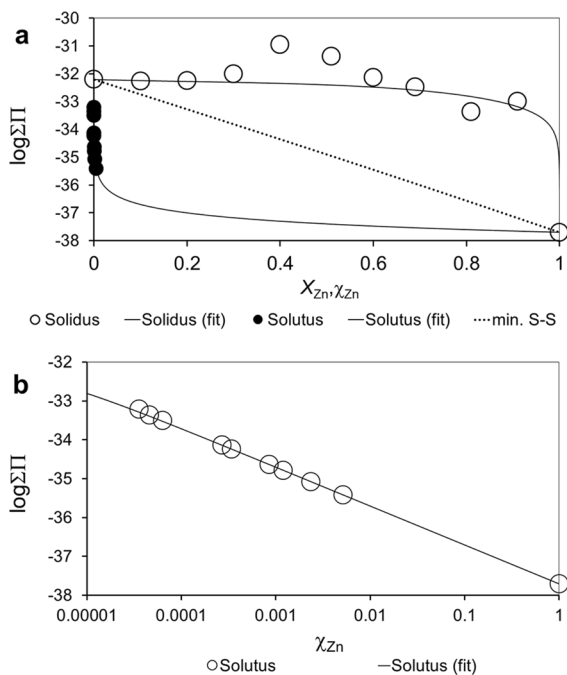


**Fig. 5** Lippmann diagram for the  $(Zn + Mg)_3Al-LDH$  system with total solubility product data for the dissolution experiments after 240 days (dots) using **a** a linear  $x$ -axis scale and **b** a logarithmic  $x$ -axis scale fitted using model solidus and solutus curves including the (dashed line) minimum stoichiometric saturation line

particular as the minor experimental scattering of the data vanished on the extended log-log scale. Unfortunately, the conode tie concept as common for phase diagrams does not work here. This is again due to the low Zn concentrations in comparison to those of Mg. The large difference between the solubility products of the endmembers involves a strong preferential partitioning of the less soluble endmember toward the solid phase, which explains why Zn-poor solid solutions are in equilibrium with Mg-rich aqueous solutions. Therefore, Zn does not play a role in equations where both cation concentrations are summed (solidus) but only in equations where both cations appear as a quotient (solutus).

The description of the thermodynamic properties of a non-ideal solid solution and consequently of the solid-phase activity coefficients requires an understanding of the excess free energy of mixing of the solid solution, i.e. of the difference between the free energy of mixing for the actual system and

an ideal solid solution, as shown below (Ganguly, 2001):

$$G^E = G^M + G^{M,id} \quad (16)$$

The Gibbs free energy of mixing  $G^M$  of a solid solution can be considered as the difference between the actual free energy of the solid solution and the free energy of a compositionally equivalent mechanical mixture of the endmember components. For an ideal binary solid solution, the free energy of mixing of endmember components  $i$  and  $j$  with the composition  $X_{i,j}$  is given by:

$$G^{M,id} = RT(X_i \ln X_i + X_j \ln X_j) \quad (17)$$

No experimental data are available, however, for the Gibbs free energies of the mixing functions for the composition of the (Mg+Zn)<sub>3</sub>-Al-LDH or, therefore, for the solid-phase activity coefficients for the system. Empirical relationships for the composition-dependence of the solid-phase activity coefficients obtained by Gibbs–Duhem integration using the Guggenheim subregular model for the excess free energy of mixing in a binary solid solution has been used successfully to fit solubility data for various binary SSAS systems (Glynn & Reardon, 1990), as shown below:

$$G^E = X_i X_j RT [\alpha_0 + \alpha_1 (X_i - X_j)] \quad (18)$$

The two dimensionless empirical coefficients  $\alpha_0$  and  $\alpha_1$  for the Guggenheim expansion equation allowed the expressions for the solid phase activity coefficients in the binary (Mg+Zn)<sub>3</sub>-Al-LDH system shown below to be derived:

$$\ln \lambda_{Mg-LDH} = X_{Zn-LDH}^2 [\alpha_0 - \alpha_1 (3 - 4X_{Zn-LDH})] \quad (19)$$

$$\ln \lambda_{Zn-LDH} = X_{Mg-LDH}^2 [\alpha_0 - \alpha_1 (4X_{Mg-LDH} - 1)] \quad (20)$$

Structural information such as mixing gaps in the binary (Mg+Zn)<sub>3</sub>-Al-LDH solid-solution behavior can be used to estimate  $\alpha_0$  and  $\alpha_1$  more accurately than the commonly used ideal solid solution assumption (i.e.  $G^M = 0$ ). The analysis results of Vegard's law presented above, however, did not indicate the presence of a miscibility gap, so a complete solid-solution series in the SSAS system was expected, i.e. the system was expected not to deviate far from the ideal system. This meant that (ignoring any difference

between activity and concentration in the aqueous phase, i.e. aqueous activity coefficient  $\gamma_{i,j} = 1$  at infinite dilution) the distribution coefficients could be defined as:

$$D = \frac{X_{Zn-LDH}/X_{Mg-LDH}}{[ZnOH^-]/[MgOH^-]} = \frac{K_{SP,Mg-LDH} \lambda_{Mg-LDH}}{K_{SP,Zn-LDH} \lambda_{Zn-LDH}} \quad (21)$$

Substitution of the definitions of the solid-phase activity coefficients  $\lambda_{Mg-LDH}$  and  $\lambda_{Zn-LDH}$  into the Guggenheim subregular model gives the expression (Glynn & Reardon, 1990):

$$D = \frac{K_{SP,Mg-LDH}}{K_{SP,Zn-LDH}} \exp [(2X_{Zn-LDH} - 1)a_0 + (6(X_{Zn-LDH}^2 - X_{Zn-LDH}) + 1)a_1] \quad (22)$$

Given the two distribution coefficients at a specified solid-solution composition, the MBSSAS code uses expressions equivalent to this equation and a Newton–Raphson procedure to calculate  $a_0$  and  $a_1$  (Glynn, 1991). The Lippmann solidus and solutus lines fitted to the present data using the MBSSAS code for  $a_0 = 0.5$  and  $a_1 = -0.5$  are shown in Fig. 5. Most of the solutus data were on a steep part of the solutus line at very low Zn concentrations. This part was, therefore, zoomed in using a logarithmic scale for the  $x$ -axis as mentioned above (Fig. 5b). The logarithmic scale solubility diagram indicated very well the excellent fit of the Lippmann equation to the experimentally acquired data according to Eq. 15, and may, therefore, be used readily to predict Zn mobility.

Having calculated  $a_0$  and  $a_1$  for the binary (Mg+Zn)<sub>3</sub>-Al-LDH solid-solution, the MBSSAS calculates (as the last step) the solid activity coefficients at infinite dilution of the respective Zn-LDH and Mg-LDH endmember components using the equations below:

$$\lambda_{Mg,XZn-LDH=1} = \exp (a_0 + a_1) = 1 \quad (23)$$

$$\lambda_{Zn,XZn=0} = \exp (a_0 - a_1) = 2.7 \quad (24)$$

These “Henry’s law activity coefficients” support the almost ideal solid-solution aqueous-solution equilibrium behavior of the binary (Mg+Zn)<sub>3</sub>Al-LDH system. The straight minimum stoichiometric saturation curve relating the

stoichiometric-saturation solubilities to the solid-solution composition is also shown in Fig. 5a (Glynn, 1991), and the equation is:

$$\Sigma\Pi_{\text{mss}} = \frac{K_{\text{SP,Mg-LDH}}^x K_{\text{SP,Zn-LDH}}^{1-x} \lambda_{\text{Mg}}^x \lambda_{\text{Zn}}^{1-x}}{X_{\text{Zn}}^{1-x} X_{\text{Mg}}^x} \quad (25)$$

The “stoichiometric saturation” concept has been introduced for kinetic dissolution experiments, in which relatively insoluble solid solutions have been found to react as physical mixtures of the end-member single-component phases over short reaction times (hours) (Plummer & Busenberg, 1987). Equation 25 gives a series of possible  $\chi_{\text{Zn,aq}}/\Sigma\Pi$  pairs that an aqueous solution may reach theoretically at stoichiometric saturation with respect to a given solid composition with a fixed  $X_{\text{Zn-LDH}}$ . This is commonly called the “equal-G curve” (Gamsjäger, 1985) but it is clearly not relevant for the present data. At longer equilibration times typical of environmental settings, a LDH solid solution reacts more like a multi-component solid and does not maintain a constant composition, as shown in the dissolution experiments. However, the minimum saturation curve may eventually become important in industrial settings, a point described in more detail by Glynn et al. (1990).

## Summary and Conclusions

Dissolution experiments using the binary (Mg+Zn)<sub>3</sub>-Al-LDH solid-solution system indicated that the solubility varied with the experimental variables (e.g. pH, Mg/Zn ratio, and reaction time). This made the system more complex and difficult to understand. A constant pH co-precipitation method was used successfully to synthesize materials with various Zn/Mg ratios, and the phase purity was assessed in each case. The samples were then equilibrated in aqueous solutions for up to 240 days. The effect of incorporation of trace Zn into the structure was to reduce significantly the aqueous solubility of the LDH. The chemical stability of the Mg-bearing hydrotalcite endmember was improved by Zn substitution for Mg in the host lattice. The solubility products were determined,

and Lippmann diagrams were constructed to analyse the SSAS equilibrium. The solutus part of the Lippmann diagram with very low  $X_{\text{Zn}}$  concentrations was enlarged for the first time using a logarithmic  $x$ -axis. This innovative approach allowed prediction of the solubility of Zn and, therefore, provided new insights into the mobilities of trace metals scavenged by LDH minerals. The SSAS model framework presented here has implications for the development of quantitative process-based thermodynamic models of trace metals immobilized in LDHs. The results are particularly relevant to remediation of trace-metal-bearing liquid waste because the metals that co-precipitated with the LDH were more strongly retained and, therefore, less soluble than the hydroxides or carbonates of the metals. The system investigated was only binary, with Zn as the only trace metal intercalated by the LDH mineral, but LDHs can be used as sorbents for various trace metals in liquid waste. Future work should address at least ternary (e.g. Mg-Zn-Cu) solid-solution systems. This could, in principle, be achieved using the same SSAS approach as described here.

**Acknowledgments** Financial support for this work was provided by the German Science Foundation (grant no. DFG KE 508/13 and 508/31). The authors thank Carolin Berg, Nora Groschopf, Suresh Kandavalli, Ralf Meffert, and Regina Walter for help in the laboratory and with drafting the methods sections.

**Funding** Open Access funding has been enabled and organized by Projekt DEAL. Funding sources are as stated in the Acknowledgments.

**Data Availability** All raw data are available from the corresponding author on reasonable request.

## Declarations

On behalf of all authors, the corresponding author approves all ethical responsibilities for publication in the journal *Clays and Clay Minerals* and consent to participate. In particular, this manuscript has not been published full or in part previously and is not submitted elsewhere or under consideration by another journal.

**Conflict of Interest** The authors declare that they have no conflict of interest.

**Open Access** This article is licensed under a Creative Commons Attribution 4.0 International License, which permits

use, sharing, adaptation, distribution and reproduction in any medium or format, as long as you give appropriate credit to the original author(s) and the source, provide a link to the Creative Commons licence, and indicate if changes were made. The images or other third party material in this article are included in the article's Creative Commons licence, unless indicated otherwise in a credit line to the material. If material is not included in the article's Creative Commons licence and your intended use is not permitted by statutory regulation or exceeds the permitted use, you will need to obtain permission directly from the copyright holder. To view a copy of this licence, visit <http://creativecommons.org/licenses/by/4.0/>.

## References

- Allada, R. K., Peltier, E., Navrotsky, A., Casey, W. H., Johnson, C. A., Berbeco, H. T., & Sparks, D. L. (2006). Calorimetric determination of the enthalpies of formation of hydroxalite-like solids and their use in the geochemical modelling of metals in natural waters. *Clays and Clay Minerals*, *54*, 409–417.
- Benito, P., Guinea, I., Labajos, F. M., Rocha, J., & Rives, V. (2008). Microwave-hydrothermally aged Zn, Al hydroxalite-like compounds: Influence of the composition and the irradiation conditions. *Microporous and Mesoporous Materials*, *110*, 292–302.
- Bocclair, J. W., & Braterman, P. S. (1999). Layered double hydroxide stability. I. Relative stabilities of layered double hydroxides and their simple counterparts. *Chemistry of Materials*, *11*, 298–302.
- Bontchev, R. P., Liu, S., Krumhansl, J. L., Voigt, J., & Nenoff, T. M. (2003). Synthesis, characterization, and ion exchange properties of hydroxalite  $Mg_6Al_2(OH)_{16}(A)_x(A')_{2-x} \cdot 4H_2O$  ( $A, A' = Cl^-, Br^-, I^-$ , and  $NO_3^-$ ,  $2 \geq x \geq 0$ ) derivatives. *Chemistry of Materials*, *19*, 3669–3675.
- Britto, S., Radha, A. V., Ravishankar, N., & Kamath, P. V. (2007). Solution decomposition of the layered double hydroxide (LDH) of Zn with Al. *Solid State Sciences*, *9*, 279–286.
- Cavani, F., Trifiro, F., & Vaccari, A. (1991). Hydroxalite-type anionic clays: Preparation, properties and applications. *Catalysis Today*, *11*, 173–301.
- Chaillot, D., Bennici, S., & Brendlé, J. (2021). Layered double hydroxides and LDH-derived materials in chosen environmental applications: a review. *Environmental Science and Pollution Research*, *28*, 24375–24405.
- Chatelet, L., Bottero, J. Y., Yvon, J., & Bouchelaghem, A. (1996). Competition between monovalent and divalent anions for calcined and uncalcined hydroxalite: Anion exchange and adsorption sites. *Colloids and Surfaces, A: Physicochemical and Engineering Aspects*, *111*, 167–175.
- Constantino, U., Vera, R. L., & Havaia, T. J. (1995). Basic properties of  $Mg^{2+}_{1-x}Al^{3+}_x$  layered double hydroxides intercalated by carbonate, hydroxide, chloride and sulfate anions. *Inorganic Chemistry*, *34*, 883–892.
- Constantino, U., Marmottini, F., Nocchetti, M., & Vivani, R. (1998). New synthetic routes to hydroxalite-like compounds - characterization and properties of the obtained materials. *European Journal of Inorganic Chemistry*, *10*(1998), 1439–1446.
- Curtius, H., Kaiser, G., Rozov, K., Neumann, A., Dardenne, K., & Bosbach, D. (2013). Preparation and characterization of Fe-, Co-, and Ni-containing Mg-Al-layered double hydroxides. *Clays and Clay Minerals*, *61*, 424–439.
- Delgado, R. R., De Pauli, C. P., Carrasco, C. B., & Avena, M. J. (2008). Influence of  $M^{II}/M^{III}$  ratio in surface-charging behaviour of Zn-Al layered double hydroxides. *Applied Clay Science*, *40*, 27–37.
- Drezdzonek, M. A. (1988). Synthesis of isopolymetalate-pillared hydroxalite via organic-anion-pillared precursors. *Inorganic Chemistry*, *27*, 4628–4632.
- Drits, V. A., & Bookin, A. S. (2006). Crystal structure and X-ray identification of layered double hydroxides. In V. Rives (Ed.), *Layered double hydroxides: present and future* (pp. 41–100). Nova Science Publishers.
- Gade, B., Heindl, A., Westermann, H., & Pöllmann, H. (2000). Secondary mineral inventory of hazardous waste landfills. In D. Rammlmair, J. Mederer, T. Oberthür, R. B. Heilmann, & H. Penttinghaus (Eds.), *Applied Mineralogy* (pp. 539–542). Balkema.
- Gamsjäger, H. (1985). Solid state chemical model for the solubility behaviour of homogeneous solid Co-Mn-carbonate mixtures. *Berichte der Bunsengesellschaft zur Physikalischen Chemie*, *89*, 1318–1322.
- Ganguly, J. (2001). Thermodynamic modelling of solid solutions. In C. A. Geiger (Ed.), *Solid Solutions in Silicate and Oxide Systems. EMU Notes in Mineralogy* (Vol. 3, pp. 37–66). Eötvös University Press.
- Glynn, P. D. (1991). MBSSAS: A code for the computation of margules parameters and equilibrium relations in binary solid-solution aqueous-solution systems. *Computers & Geosciences*, *17*, 907–966.
- Glynn, P. D., & Reardon, E. J. (1990). Solid-solution aqueous-solution equilibria: thermodynamic theory and representation. *American Journal of Science*, *290*, 164–201.
- Glynn, P. D., Reardon, E. J., Plummer, L. N., & Busenberg, E. (1990). Reaction paths and equilibrium end-points in solid-solution aqueous-solution systems. *Geochimica et Cosmochimica Acta*, *54*, 267–282.
- Guilbaud, R., White, M. L., & Poulton, S. W. (2013). Surface charge and growth of sulfate and carbonate green rust in aqueous media. *Geochimica et Cosmochimica Acta*, *108*, 141–153.
- Gustafsson, J.-P. (2020). Visual MINTEQ version 3.1. <https://vminteq.lwr.kth.se/download/>. Accessed July 2021
- Hofmeister, W., & Von Platen, H. (1992). Crystal chemistry and atomic order in brucite-related double-layer structures. *Crystallography Reviews*, *3*, 3–29.
- Johnson, C. A., & Glasser, F. P. (2003). Hydroxalite-like minerals  $(M_2Al(OH)_6(CO_3)_{0.5} \cdot xH_2O)$ , where  $M=Mg, Zn, Co, Ni$  in the environment: Synthesis, characterization and



- thermodynamic stability. *Clays and Clay Minerals*, 51, 1–8.
- Juan, J. B., Páez-Mozo, E. A., & Ted, O. S. (2004). Models for the estimation of thermodynamic properties of layered double hydroxides: Application to the study of their anion exchange characteristics. *Química Nova*, 27, 601–614.
- Klopprogge, J. T., Hickey, L., & Frost, R. L. (2004). The effects of synthesis pH and hydrothermal treatment on the formation of zinc aluminium hydroxalicates. *Journal of Solid State Chemistry*, 177, 4047–4057.
- Kulik, D. A., & Kersten, M. (2002). Aqueous solubility diagrams for cementitious waste stabilization systems. 4. A carbonation model for Zn-doped calcium silicate hydrate by Gibbs energy minimization. *Environmental Science & Technology*, 36, 2926–2931.
- Lippmann, F. (1980). Phase diagrams depicting aqueous solubility of binary mineral systems. *Journal of Mineralogy and Geochemistry*, 139, 1–25.
- Meyn, M., Beneke, K., & Lagaly, G. (1990). Anion-exchange reactions of layered double hydroxides. *Inorganic Chemistry*, 29, 5201–5207.
- Miyata, S. (1983). Anion-exchange properties of hydroxalicate-like compounds. *Clays and Clay Minerals*, 31, 305–311.
- Plummer, L. N., & Busenberg, E. (1987). Thermodynamics of aragonite-strontianite solid solutions: results from stoichiometric dissolution at 25 and 76°C. *Geochimica et Cosmochimica Acta*, 51, 1393–1411.
- Ren, C., Zhou, M., Liu, Z., Liang, L., Li, X., Lu, X., Wang, H., Ji, J., Peng, L., Hou, G., & Li, W. (2021). Enhanced fluoride uptake by layered double hydroxides under alkaline conditions: Solid-state NMR evidence of the role of surface >MgOH sites. *Environmental Science & Technology*, 55 (22), 15082–15089. <https://doi.org/10.1021/acs.est.1c01247>
- Rozov, K. B., Berner, U., Kulik, D. A., & Diamond, L. W. (2011). Solubility and thermodynamic properties of carbonate-bearing hydroxalicate-pyroaurite solid solutions with a 3:1 Mg/(Al+Fe) mole ratio. *Clays and Clay Minerals*, 59, 215–232.
- Shannon, R. D. (1976). Revised effective ionic radii and systematic studies of interatomic distances in halides and chalcogenides. *Acta Crystallographica Section A*, 32, 751–767.
- Taylor, H.F.W. (1973). Crystal structures of some double hydroxide minerals. *Mineralogical Magazine*, 39, 377–389.
- Theiss, F. L., Ayoko, G. A., & Frost, R. L. (2016). Synthesis of layered double hydroxides containing Mg<sup>2+</sup>, Zn<sup>2+</sup>, Ca<sup>2+</sup> and Al<sup>3+</sup> layer cations by co-precipitation methods – A review. *Applied Surface Science*, 383, 200–213.
- Trolard, F., & Bourrié, G. (2012). Fougerite a natural layered double hydroxide in Gley soil: Habitus, structure, and some properties. *Intech Open Science Chapter*, 9, 171–188. <https://doi.org/10.5772/50211>
- Ulibarri, M. A., & Hermosín, M. C. (2006). Layered double hydroxides in water decontamination. In V. Rives (Ed.), *Layered double hydroxides: present and future* (pp. 285–321). Nova Science Publishers.
- Velu, S., Ramkumar, V., Narayanan, A., & Swamy, C. S. (1997). Effect of interlayer anions on the physicochemical properties of zinc-aluminium hydroxalicate-like compounds. *Journal of Materials Science*, 32, 957–964.